Published in final edited form as:

*Ultrasound Med Biol*. 2016 March ; 42(3): 769–781. doi:10.1016/j.ultrasmedbio.2015.10.015.

# Molecular acoustic angiography: a new technique for high resolution superharmonic ultrasound molecular imaging

**Sarah E. Shelton**[*,1], **Brooks D. Lindsey**[*,1], **James K. Tsuruta**[2], **F. Stuart Foster**[3], and **Paul A. Dayton**[1,4]

[1]Joint Department of Biomedical Engineering, University of North Carolina at Chapel Hill and North Carolina State University, CB7575, Chapel Hill, NC 27599

[2]Department of Pediatrics, University of North Carolina at Chapel Hill, CB7220, Chapel Hill, NC 27599

[3]Department of Medical Biophysics, Sunnybrook Health Sciences Centre, Toronto, ON, Canada

[4]Biomedical Research Imaging Center, University of North Carolina at Chapel Hill, Marsico Hall, Chapel Hill, NC 27599

## Abstract

Ultrasound molecular imaging utilizes targeted microbubbles to bind to vascular targets such as integrins, selectins, and other extracellular binding domains. After binding, these microbubbles are typically imaged using low pressures and multi-pulse imaging sequences. In this article, we present an alternative approach for molecular imaging using ultrasound which relies on superharmonic signals produced by microbubble contrast agents. Bound bubbles were insonified near resonance using a low frequency (4 MHz) and superharmonic echoes were received at high frequencies (25–30 MHz). While this approach was observed to produce declining image intensity during repeated imaging in both *in vitro* and *in vivo* experiments due to bubble destruction, the feasibility of superharmonic molecular imaging was demonstrated for transmit pressures which are sufficiently high to induce shell disruption in bound microbubbles. This approach was validated using microbubbles targeted to the $\alpha_v\beta_3$ integrin in a rat fibrosarcoma model (n=5), and combined with superharmonic images of free microbubbles to produce high contrast, high resolution 3D volumes of both microvascular anatomy and molecular targeting. Image intensity over repeated scans and the effect of microbubble diameter were also assessed *in vivo*, indicating that larger microbubbles yield increased persistence in image intensity. Using ultrasound-based acoustic angiography images rather than conventional B-mode ultrasound to provide the underlying anatomical information facilitates anatomical localization of molecular markers. Quantitative analysis of relationships between microvasculature and targeting information indicated that most targeting occurred within 50 μm of a resolvable vessel (>100 μm diameter). The combined

Corresponding author: Paul Dayton, Ph.D., UNC-NCSU Joint Department of Biomedical Engineering, 152 MacNider Hall, CB7575, Chapel Hill, NC, 27599, phone: (919) 843 9521, fax: (919) 843 9520, padayton@email.unc.edu.

*These authors contributed equally to this work

information provided by these scans may present new opportunities for analyzing relationships between microvascular anatomy and vascular targets, subject only to limitations of the current mechanically-scanned system and microbubble persistence to repeated imaging at moderate mechanical indices.

**Keywords**

microbubble; targeted imaging; angiogenesis; microvasculature; biomarker

## Introduction

In contrast to anatomical imaging methods, molecular imaging reveals functional information about tissue pathophysiology based on the accumulation of a molecular tracer. However, the value of a molecular imaging technique is often greatly enhanced by combining it with anatomical imaging in order to visualize the distribution of the marker. Clinically, this approach is used in systems combining computed tomography with positron emission tomography (PET-CT) or single photon emission computed tomography (SPECT-CT). These combined systems have demonstrated higher accuracy in localizing abnormalities, often resulting in changes in treatment plans in cancers of the lung, thyroid, breast, and prostate (Cerfolio et al. 2004; Tharp et al. 2004; Roach et al. 2006; Lerman et al. 2007; Garami et al. 2012; Soyka et al. 2012). In ultrasound molecular imaging, images of targeted microbubble contrast agent are typically overlaid on anatomical B-mode images to allow visualization of the spatial distribution of markers. Due to the intravascular nature of microbubbles, they are particularly well-suited to the study of endothelial markers of disease. For this reason, many recent studies in ultrasound molecular imaging have investigated angiogenesis and related processes of vascular remodeling and inflammation (Kaufmann and Lindner 2007; Voigt 2009; Anderson et al. 2011; Inaba and Lindner 2012; Hyvelin et al. 2014; Wang et al. 2014).

While ultrasound possesses advantages over other molecular imaging modalities due to its relatively low cost, portability, and lack of ionizing radiation, it also has limited penetration depth at the high frequencies required to achieve sub-millimeter resolution. In addition, the ultrasound image providing anatomy is quite different in nature from CT or magnetic resonance imaging (MRI) images that provide anatomical information for PET or SPECT, as contrast in B-mode ultrasound images is the result of differences in acoustic backscattering from tissue, and depends on the size, distribution, and acoustic impedance of the scatterers. Ultrasound also has a limited field of view compared to whole-body imaging modalities. The development of microbubble contrast agents, which provide substantially higher levels of acoustic scattering relative to erythrocytes, has greatly enhanced the ability to use ultrasound to image both vascular anatomy and blood flow dynamics. Contrast-enhanced ultrasound (CEUS) imaging with high frequency transducers has allowed imaging of small vessels with resolutions on the order of a few hundred microns, providing potential for assessing angiogenesis and vascular remodeling with both targeted and non-targeted microbubbles (Ellegala et al. 2003; Leong-Poi et al. 2005; Liu et al. 2008; Willmann et al. 2008; Willmann et al. 2010; Pysz et al. 2011; Wang et al. 2015a). High-resolution molecular

imaging is particularly valuable for pre-clinical imaging in small animal models and studies in which small anatomical locations are of interest, although high frequency contrast-specific imaging is technically challenging to implement (Rychak et al. 2007; Foster et al. 2009; Foster et al. 2011; Yan et al. 2012; Denbeigh et al. 2014; Liu et al. 2015).

An alternative approach to high frequency CEUS involves the use of dual-frequency transducers, with a low frequency transmit pulse used to excite microbubbles near their resonance and a high frequency element receiving only higher harmonic echoes produced by microbubbles (Gessner et al. 2010). Detection of these “superharmonic” signals produced by microbubbles with multi-frequency transducers was first reported by Bouakaz et al. (Bouakaz et al. 2003) and by Kruse and Ferrara (Kruse and Ferrara 2005), although these early investigators did not use this technology to develop the 3-D microvessel images demonstrated more recently by Gessner et al. (Gessner et al. 2013). The “transmit low/receive high” dual-frequency approach has previously been utilized in molecular imaging by Ferrara et al. (Hu et al. 2010; Hu et al. 2013). When transmitting at 2 MHz and receiving at 15 MHz, Hu et al. demonstrated approximately a two-fold improvement in spatial resolution *in vitro* relative to multi-pulse techniques employed by commercial scanners (Hu et al. 2013). The use of a low transmit frequency improves the penetration depth relative to contrast imaging at a single high frequency. For example, at a depth of 1.5 cm and an attenuation of 0.2 dB/cm/MHz, two-way attenuation in a 25 MHz scan is 15 dB but is only 8.7 dB with a 4/25 MHz dual-frequency scan. Transmitting at a lower frequency also more closely corresponds to the resonance frequencies of most commercially-available microbubble contrast agents (Doinikov et al. 2009; Faez et al. 2011; Helfield and Goertz 2013), improving image contrast, which is vital in molecular imaging when relatively few microbubbles are typically present.

Using this “transmit low/receive high” approach with prototype dual-frequency, mechanically-steered transducers connected to a commercial ultrasound system, we have recently demonstrated the ability to form high resolution images of vasculature with resolutions of approximately 150 μm and with almost no tissue interference. We call this technique “acoustic angiography” due to the images’ similarity to CT or MR angiography. While commercial ultrasound scanners perform contrast-specific imaging within a single transducer bandwidth, our approach forms images using only received signals at frequencies at least three times higher than the transmitted frequency. Our group recently found that using a receiving center frequency at least three times higher than the transmit center frequency produces the highest contrast-to-tissue ratios, as tissue amplitudes decrease more rapidly than microbubbles amplitudes with increasing frequency (Lindsey et al. 2014). In addition, while using higher harmonics to form images (i.e. $5^{th}$ rather than $3^{rd}$) may further reduce sensitivity, it provides the increased resolution necessary for resolving vasculature <300 μm in diameter. Using these 3-D imaging volumes and quantitative metrics of vascular signatures, we have further demonstrated the ability to distinguish between healthy and cancerous tissues (Gessner et al. 2012a; Shelton et al. 2015). High specificity to contrast due to transmitting at low frequencies and receiving at much higher frequencies allows suppression of tissue artifact while preserving frame rates without requiring a separate control image to be acquired and subtracted. This simplifies the imaging protocol and

eliminates artifacts due to physiological motion or misregistration of the control and contrast images.

Several studies have found that another means for improving the sensitivity of ultrasound molecular imaging is by adjusting the size distribution of the microbubble population (Talu et al. 2007; Sirsi et al. 2010; Streeter et al. 2010). In dual-frequency superharmonic imaging, we have recently observed that using a population with larger microbubbles results in superharmonic signals with increased amplitude (Lindsey et al. 2014). This effect arises because larger microbubbles are capable of producing superharmonic signals over a greater number of acoustic pulses (Lindsey et al. 2015).

Despite the promising resolution of dual-frequency superharmonic imaging, our own recent studies indicate that dual-frequency superharmonic imaging is at least partially destructive to microbubbles (Lindsey et al. 2015), which makes implementation of superharmonic molecular imaging a significant challenge. The dual-frequency transducer design is critical for separation of tissue and microbubble echoes, as a wide separation between transmit and receive bandwidths ensures that only microbubble echoes are received at the higher frequencies. However, the focal spot is larger for the low frequency element than the high frequency element. The result is that as both transducers are swept in unison to form a 2-D image, a stationary microbubble is subjected to multiple off-axis, low frequency transmit pulses before the center of the dual low- and high- frequency focus is aligned to the microbubble. While many commercially-available systems utilize techniques such as synthetic aperture processing and broad beam insonation to ensure uniform acoustic intensity over wide regions of interest for microbubble imaging (Brock-Fisher et al. 1996), the transducers utilized by these systems do not have the necessary bandwidth to perform the superharmonic contrast imaging enabled by the described prototype transducer.

Although the mechanical indices used in superharmonic imaging are below the maximum of 0.8 for which safety has been evaluated for Definity® (Lantheus Medical Imaging, N. Billerica, MA)(Imaging 2013), our previous studies indicate that microbubble shell disruption is required to produce superharmonic signals (approximately 300 kPa or greater at 4 MHz)(Lindsey et al. 2015), which may present a challenge for molecular imaging if bound microbubbles might be destroyed before the superharmonic signal they produce can be detected. Fortunately, there is evidence that the same microbubbles can produce superharmonic echoes in response to multiple insonations (Kruse and Ferrara 2005; Lindsey et al. 2015), suggesting that it may be possible to balance production of superharmonic signals and microbubble destruction in such a way as to enable molecular imaging.

In this article, we describe the development of an approach for high resolution molecular imaging based on microbubble superharmonic echoes. This technique uses spectrally separated transmit and receive bandwidths to form images of bound microbubbles rather than the low-mechanical index multi-pulse sequences that are commonly used (Phillips 2001). Intensity and persistence of the superharmonic signals in these images were evaluated through *in vitro* experiments in micro-cellulose tubes and *in vivo* imaging studies in a subcutaneous tumor model. When combined with a sequentially-acquired acoustic angiography volume, the developed approach provides simultaneous 3-D visualization of

both microvascular structure and molecular markers of angiogenesis with unprecedented resolution. While the B-mode ultrasound images which typically provide anatomical information in ultrasound molecular imaging are difficult to display in 3D and require an experienced user to understand and interpret differences between tissue types, the vascular anatomy provided by acoustic angiography can be easily displayed in 3D and may be readily interpreted by users with limited previous ultrasound experience. Finally, microvascular information in the acoustic angiography volume can be analyzed using metrics such as vascular density (Dunleavey et al. 2014) or tortuosity to quantitatively assess vascular remodeling (Gessner et al. 2012a; Shelton et al. 2015). When combined with molecular targeting information, this may provide new information regarding the spatial distribution of vascular biomarkers.

## Materials and Methods

Acoustic angiography imaging experiments were performed with modified VisualSonics RMV probes and a Vevo 770 ultrasound scanner (VisualSonics, Toronto, Canada). In this work, modified RMV710B (25 MHz center frequency) and RMV707 (30 MHz center frequency) transducers were used, each with an additional 4 MHz annular element which is confocal to the high frequency element (Gessner et al. 2010). The low frequency element is used only for transmitting, while the high frequency element only receives higher harmonics produced by microbubbles. The two single-element transducers are mechanically steered to acquire a 2-D image and can be translated using a motion stage to combine multiple 2-D images into volumetric data.

### Microbubble preparation for *in vitro* studies

Lipid solutions (Streeter et al. 2010) were formulated with a 9:1 molar ratio of 1,2-distearoyl-*sn*-glycero-3-phosphocholine (DSPC) and 1,2-distearoyl-*sn*-glycero-3-phosphoethanolamine-N-methoxy (polyethylene–glycol)-2000 (DSPE-PEG2000) (Avanti Polar Lipids, Alabaster, AL) in a solution containing propylene glycol 15% (v/v), glycerol 5% (v/v), and phosphate-buffered saline (PBS) 80% (v/v). 1.5 mL aliquots of this lipid solution were placed in sealed 3 mL glass vials and the air headspace was exchanged with decafluorobutane (DFB) gas purchased from Fluoromed (Round Rock, TX, USA). Microbubbles with DFB gas cores and phospholipid shells formed spontaneously when agitated in a Vialmix device (Lantheus Medical Imaging, N. Billerica, MA). The concentration, and diameter of microbubbles in this emulsion was measured via (single particle) optical techniques (Accusizer 780, Particle Sizing Systems, Santa Barbara, CA, USA) (Satinover et al. 2014). For targeted bubbles, a biotinylated PEG was used (DSPE-PEG2000-Biotin) (Zhao et al. 2004) to replace 50% of the DSPE-PEG2000. Microbubble emulsions were washed with four centrifugations, and produced a stable population of microbubbles with a diameter of approximately 1.4 μm (Feshitan et al. 2009).

### *In vitro* experiments

Transducer calibration and spatial mapping of the low frequency transmit beam was performed with a calibrated needle hydrophone (HNA 0400, Onda Corp., Sunnyvale, CA) on a computerized motion stage (Newport XPS, Irvine, CA) and digitized using a digital

acquisition board (Signatec PDA14, Corona, CA). The hydrophone was positioned at the focus of the transducer and translated laterally to measure a 4 mm extent of the beam profile at the focal depth (15 mm for RMV 710B). In acoustic angiography the resolution is primarily dictated by the high frequency receiving transducer, and we have recently characterized axial resolution for microbubble superharmonic imaging at across a wide range of frequencies (Lindsey et al. 2014). Relative to the study of Hu et al. (Hu et al. 2013), our own data indicate that axial resolution might be expected to decrease from ~250 μm at frequencies of 2/15 MHz to ~170 μm at 4/25 MHz, providing slightly improved resolution, though contrast-to-tissue ratio is expected to decrease with increasing receiving frequency. Therefore, line spacing in a 2-D image is determined by the resolution of the high frequency element. Manufacturer-provide information on scan geometry was used to compute line spacing at the focus (43 μm) in order to determine the overlap of the low frequency transmit pulse in adjacent lines.

*In vitro* microbubble targeting was achieved using biotinylated microbubbles and an avidin-coated cellulose tube. First, the 200 μm (inner diameter) cellulose tube (Spectrum Labs, Rancho Dominguez, CA) was infused with 100% ethanol, which was then cleared by filling the tube with air. Next the tube was filled with a 5 mg/mL solution of avidin (Sigma-Aldrich, St. Louis, MO) in phosphate-buffered saline (PBS) and allowed to sit at room temperature for 30 minutes before being flushed with PBS and positioned in a water bath at the focus of the dual-frequency transducer. An infusion of $5\times10^4$ biotin-coated microbubbles in 300 μL of PBS was pumped through the tube at a rate of 30 μL/min (Harvard Apparatus PHD2000, Holliston, MA), followed by a 10 min flush of pure PBS to remove any unbound microbubbles. 2-D images of the bound microbubbles were acquired for 100 frames at a frame rate of 1 Hz at peak negative pressures of 200, 350, and 500 kPa. Then, image clips were exported and analyzed in ImageJ (U. S. National Institutes of Health, Bethesda, MD). An image of the tube prior to contrast infusion was subtracted from each set of acquired images to eliminate any non-microbubble artifacts, then a region of interest was defined around the tube to compute image intensity. Experiments were repeated in triplicate and results were averaged together for each transmit pressure tested. A new tube was prepared with a new microbubble injection for each trial.

### Microbubble preparation for *in vivo* studies

Microbubbles targeted to the $\alpha_v\beta_3$ integrin were created with an 18:1:1 molar ratio of DSPC, DSPE-PEG2000, and DSPE-PEG2000-maleimide cross-linked to the peptide Cyclo-Arg-Gly-Asp-D-Tyr-Cys (cyclic RGD, Peptides International - Louisville, KY) in phosphate-buffered saline (PBS) (Fisher Scientific, Pittsburgh, PA). The cyclic RGD peptide targets vessels expressing $\alpha_v\beta_3$ integrin, which is characteristic of angiogenic tumors (Ellegala et al. 2003; Leong-Poi et al. 2003; Dayton et al. 2004; Streeter et al. 2010; Anderson et al. 2011; Streeter et al. 2011; Hu et al. 2013).

Previous investigations of the relationship between microbubble diameter and molecular imaging (Streeter et al. 2010) and contrast-to-tissue ratio in acoustic angiography imaging (Lindsey et al. 2014) both demonstrated improved performance for bubbles having diameters in the range of 3–4 μm rather than 1–2 μm. Additionally, larger bubbles are likely to produce

superharmonic signals over a greater number of pulses than smaller bubbles (Lindsey et al. 2015). In order to examine the effect of microbubble diameter on superharmonic imaging *in vivo*, two populations of microbubbles were prepared: a polydisperse population as described in our *in vitro* studies with a mode diameter of approximately 1.4 μm, and larger diameter microbubbles enriched using differential centrifugal separation (Feshitan et al. 2009; Streeter et al. 2010) with a mode diameter of approximately 3.8 μm.

## Animal care and imaging

The Fisher 344 fibrosarcoma (FSA) model was prepared as previously described (Yuan et al. 2006). *In vivo* imaging occurred when tumors reached approximately 1 cm in diameter. Rats were anesthetized with vaporized isoflurane and oxygen, and a 24 gauge catheter was inserted into the tail vein. Fur was removed from the imaging region by shaving and chemical depilation, and ultrasound gel was applied to the skin. Body temperature was maintained throughout using a heated imaging stage, and rats were secured to the imaging platform with surgical tape to minimize motion during the study. Acquisition times were less than 1 minute for the molecular volume and between 1 and 2 minutes for the microvascular volume. All animal experiments were performed in accordance with The University of North Carolina at Chapel Hill Institutional Animal Care and Use Committee.

Using the same VisualSonics 770 system and prototype transducer, tumor location was first identified in high frequency B-mode imaging. Next, a dual-frequency image was acquired prior to contrast agent administration for identification of any tissue artifacts. A bolus of $5\times10^7$ cyclic RGD microbubbles was injected through the tail-vein catheter. After a 12 minute wait, circulating microbubbles had cleared, and 3-D images of targeted microbubbles were acquired in dual-frequency mode with a step size of 250 μm between 2D images to avoid destroying bubbles in the adjacent imaging plane. The 12 minute wait for targeting is similar to that used in previous ultrasound molecular imaging studies (Kaufmann et al. 2007; Inaba and Lindner 2012; Wang et al. 2015b) and was determined based on prior scanning of two animals in which the degree of free bubbles in circulation was assessed every 4 minutes post-injection for 28 min. To test the expected improvement due to increased microbubble diameter, molecular imaging scans were acquired consecutively with size sorted (larger) and polydisperse (smaller) microbubbles in the same animal, with any remaining bound microbubbles destroyed between bolus injections by performing a scan at a peak negative pressure of 1400 kPa. The order in which the pressures were tested was randomized in order mitigate any potential effects of repeated boluses, which are expected to be negligible (Streeter and Dayton 2013). To examine microbubble destruction over repeated imaging, four 3-D scans were acquired at each set of parameters (microbubble diameter, pressure). Following the acquisition of molecular images, conventional dual-frequency acoustic angiography images were acquired using a constant infusion of $1.5\times10^8$ untargeted microbubbles/min, a peak negative pressure of 1.2 MPa, and a step size of 100 μm between 2D images.

## Image processing and analysis

Volumetric image data of targeted microbubbles were imported into ImageJ, and background noise was reduced by subtracting the background using the “rolling ball” algorithm with a

radius of 30 (Sternberg 1983). Tissue signal was reduced by subtracting a volume acquired before contrast agent injection. In MATLAB (The MathWorks Inc., Natick, MA), thresholding was applied to remove any remaining noise. The image intensities in volumetric tumor regions were calculated for each scan, and the average intensity of successive scans were normalized to the first scan in order to compare the relative loss of signal due to microbubble destruction. Acoustic angiography and molecular imaging volumes for the same animals were combined into a single volume in ImageJ by inserting blank frames into the molecular imaging volumes so that the slice spacing matched that of the acoustic angiography volumes, then merging the two volumes using different colors, with acoustic angiography data displayed in white and targeting information displayed in green.

For n=5 animals, individual vessels were segmented from acoustic angiography image volumes using centerline extraction via height ridge traversal with manually defined seed points (Aylward and Bullitt 2002). Coordinates of segmented vessels as well as coordinates and voxel intensities of the targeting sites from the molecular imaging data were read into MATLAB. Vessel coordinates were down-sampled to match the image spacing of the molecular imaging data. In order to analyze spatial relationships between resolvable vessels and targeted microbubble signal, distances between the targeting site and the five closest vessels were computed for each targeting site. Any registration artifacts due to differences in respiratory motion between sequential scans were assumed to be negligible. Previous studies indicate that the mean root-mean-square (RMS) error between two consecutive frames due to physiological motion is 7.2 ± 3.3 μm. Vessel diameters for these five closest vessels were also recorded for each targeting site.

## Results

### In vitro

Transmit pressure profiles were created at peak negative pressures of 200, 350, and 500 kPa at 4 MHz (Figure 1A) in order to visualize pressure levels incident on neighboring microbubbles from a single low frequency transmit event. With a mechanically-steered transducer, a single microbubble in the field is subject to increasing pressures from the low frequency element as the transducer arm moves towards the microbubble. Thus by the time both the peak transmit pressure and the focus of the high frequency receive element are aligned to the microbubble for acquisition of the imaging line, the microbubble has already experienced several pulses at increasing pressures. Figure 1B contains a diagram describing the motion of the transducer across ten imaging lines occupying 388 μm of the image in the lateral direction (only three transducer positions are shown instead of ten for clarity). A single microbubble positioned at the location of line 10 receives gradually increasing pressures with each transmit pulse as the transducer moves from line 1 to line 10. Figure 2 depicts this overlapping spacing of the ten low frequency transmit pulses for the 350 kPa case. Vertical lines delineate the transmit line spacing of 43.1 μm and horizontal lines show the magnitude of negative pressure experienced by a bubble at location zero (in focus at line 10) for preceding transmit events.

Bound microbubbles in cellulose tubes were observed over 100 frames to assess frame-to-frame decreases in signal intensity due to microbubble destruction by the transmit pulses (Figure 3). As expected, initial intensity of the targeted microbubble signal is directly related to the peak negative pressure of the transmit pulse. All three pressures (200, 350 and 500 kPa, peak negative pressure) demonstrated some loss of signal from the initial transmit pulse, likely due to the preferential destruction of small microbubbles (Lindsey et al. 2015). However, observations at 200 and 350 kPa indicate relatively slow decline in microbubble signal, with a greater decrease in intensity observed for the 500 kPa test case. At the lowest pressure (200 kPa), the bound microbubble signal remained relatively stable across the 100 transmit pulses, indicating minimal destruction. However, the intensities of the superharmonic echoes received by the high frequency element were low for the 200 kPa transmit pressure case. At the highest pressure (500 kPa), average intensity decreased quickly in the first few frames, and then decayed slowly over approximately frames 10–100. With the moderate pressure (350 kPa), the intensity decreased gradually over all 100 frames and exhibited greater microbubble signal than the observations at 200 and 500 kPa by frame 3. Overall, *in vitro* results indicated that a balance between microbubble destruction and generation of broadband superharmonic signals might be achievable for bound microbubbles for *in vivo* molecular imaging.

## In vivo

Imaging of microbubbles targeted to the $\alpha_v\beta_3$ integrin demonstrated little to no detectable signal *in vivo* at the low peak negative pressures examined *in vitro*. Therefore, the pressures tested were increased to non-derated values of 700, 900, and 1200 kPa. Several reasons account for the need for greatly increased pressures *in vivo*, including attenuation, small vessel confinement effects, and blood viscosity. For example, for an imaging depth of 15 mm, an attenuation of 0.2 dB/cm/MHz in overlying tissues represents a loss of 1.2 dB at 4 MHz. Superharmonic signals from the relatively few bubbles under the high frequency focus are also difficult to detect at the transducer, as the same attenuation of 0.2 dB/cm/MHz results in attenuations of 9 dB at 30 MHz. Additionally, Caskey et al. have reported that microbubble oscillation is constrained when bubbles are confined to smaller vessels *in vivo*, measuring a relative expansion of a factor of 4–11.5 in 200 μm-inner diameter tubes *in vitro* as compared to a mean relative expansion of 1.5 in *ex vivo* vessels less than 30 μm in diameter (Caskey et al. 2007). This may indicate higher pressures are required to produce superharmonic signals in small vessels. Other authors have investigated the effect of blood viscosity on microbubble oscillation, finding that microbubble resonance is severely altered in the presence of viscous damping (Khismatullin 2004; Sassaroli and Hynynen 2004).

With these higher pressures, it was possible to create *in vivo* images of bound microbubbles which could be overlaid on acoustic angiography image volumes as a reference for vascular structure. Note that these molecular imaging volumes could also be overlaid on B-mode images, as is customary in ultrasound molecular imaging. Figure 4 shows fused maximum intensity projections of molecular and acoustic angiography images in the lateral view (4A) and dorsal-ventral view (4B) of a tumor approximately 1 cm in diameter, using a polydisperse population of microbubbles (1–2 μm diameter) and a peak negative pressure of 1200 kPa. The relative decrease in image intensity over four successive scans in the same

five animals for both sorted or polydisperse microbubble populations is shown in Figure 5. During the first scan, the larger sorted microbubbles were clearly brighter than the first scan of the polydisperse population, but the difference between the signal from each population decreased through scan 4, when neither microbubble population yielded significant detectable signal at a transmit peak negative pressure of 1200 kPa.

In comparing image intensity for the size-sorted microbubbles at pressures of 700, 900, and 1200 kPa in the same animal, the higher pressures were found to produce the greatest image intensity from bound microbubbles. Figure 6 shows example image overlays of acoustic angiography and molecular imaging at the three pressures tested in a single representative animal. At higher pressures, both the brightness of individual targeting sites and the number of detectable targeting sites were visibly greater. The relative image intensities of the 3 different peak negative insonation pressures were computed across four scans until very little signal was detectable at any pressure, and this data is shown in Figure 7 for all 5 animals. The plot in Figure 7 shows that the mean image intensity in targeted microbubble images at 700 kPa is fairly constant over four scans, although the mean image intensity value is low. At higher pressures, the mean initial intensity of scan 1 improved, but there was a greater decline in image intensity with each successive scan. The greatest targeting signal intensity resulted from the first scan at 1200 kPa, the highest peak negative pressure tested.

Segmentation of vessels visible in acoustic angiography images acquired with a constant infusion of microbubbles allowed comparison of the spatial distribution of targeted microbubbles and vascular structure. Following segmentation, distances from each targeting site to the 5 nearest vessels and the diameters of those vessels were computed in MATLAB (see Figure 8). The majority of targeting sites were within 50 μm of the centerline of a resolvable vessel, and very few targeting sites were located farther than 150 μm from a segmented vessel (Figure 8A). Additionally, we observed that the majority of targeting occurred in small vessels. Figure 8B shows that $\alpha_v\beta_3$ targeting increased as vessels decreased in diameter, with a decline in the percentage of targeting sites located in or near vessels 100–200 μm in diameter, which is approximately the resolution limit of the acoustic angiography images. The relationship between vessel diameter and levels of targeted microbubble detection may be related to purely physical implications of smaller diameter vessels, or to patterns of $\alpha_v\beta_3$ integrin expression.

## Discussion

### Bubble destruction and superharmonic molecular imaging

In this article we have demonstrated the feasibility of forming high resolution images of microbubbles targeted to the $\alpha_v\beta_3$ integrin using an imaging technique which forms images of only the superharmonic echoes of microbubbles. While this technique is known to be partially destructive, bound microbubbles persisted sufficiently long *in vivo* to allow for the formation of high resolution superharmonic molecular images (Figure 4). Although image intensity decreased rapidly with each subsequent scan (Figure 5, Figure 7), superharmonic echoes were detectable on the initial scan despite the fact that microbubbles had already been subjected to multiple pulses due to the large focal size of the low frequency transducer element (Figure 1–2). This partial persistence of superharmonic signals over a few pulses is

consistent with the *in vitro* studies reported here (Figure 3) and previously (Lindsey et al. 2015). We have also observed that superharmonic molecular imaging may be enhanced by using a microbubble population with a slightly larger diameter, consistent with previous observations that larger microbubbles improve sensitivity in conventional molecular imaging (Talu et al. 2007; Streeter et al. 2010) and in superharmonic imaging of free bubbles (Lindsey et al. 2014), and that larger free microbubbles are more prone to deflation over several pulses relative to smaller microbubbles (Lindsey et al. 2015). While microbubble persistence is clearly a challenge for this technique, acquiring useful superharmonic molecular images is possible on at least the first acquisition and appears to be aided by the use of microbubbles having slightly larger diameters. In addition, the use of higher microbubble concentrations might produce increased targeting more similar to conventional ultrasound molecular imaging approaches, but the current concentration allows spatial comparison between molecular and microvascular imaging volumes.

## Potential improvements

While superharmonic molecular images with the highest image intensity were acquired with the highest pressure tested (1200 kPa), opportunities may remain for further optimization of transmit frequencies or pressures in order to either increase sensitivity of the initial scan or prolong the usefulness of the images over a greater number of scans. The effects of the *in vivo* environment on microbubble oscillation have not been precisely quantified, so the peak negative pressure required to induce microbubble deflation or destruction *in vivo* are unclear. Previous studies have reported that microbubbles persist longer as vessel size decreases (Caskey et al. 2007), however greater pressures may be required to produce superharmonic echoes from these bubbles. This suggests that in a field of view filled with vessels of varying diameter, microbubble oscillation and thus received signal may depend on vessel diameter. Thus sensitivity to smaller vessels may not be limited merely by the presence of fewer microbubbles or slower reperfusion rates in these vessels.

Due to the mechanical steering of the prototype transducer, each microbubble is subjected to many lower pressure pulses before the receiving focus is aligned over the microbubble. Additionally, bound microbubbles are subject to secondary Bjerknes forces which may cause detachment of bound microbubbles at low MI (Garbin et al. 2011; Gessner et al. 2012b; Loughran et al. 2012). These forces may induce microbubble unbinding in this method due to lower pressure pulses acting on a microbubble before the dual focus is aligned with the microbubble, potentially reducing sensitivity if detached microbubbles flow out of plane before being detected. Both of these effects (destruction and detachment of microbubbles outside of the receiving focus) could be mitigated by using a transducer having transmit and receive foci which were more similar in size, as the lateral resolution of the high frequency element is 140 μm (710B) while that of the low frequency element is ~1 mm. Alternatively, a dual-frequency array transducer would allow all echoes to be received by the high frequency array even with a large transmit focus (Bouakaz et al. 2002; Stephens et al. 2006; Martin et al. 2014).

Use of an array would also help mitigate any effects of motion artifacts in the spatial comparison between vascular and molecular imaging data by allowing increased acquisition

rates and providing a more uniform acoustic field. However, because vessel centerlines are extracted using the described segmentation technique, single frame shift errors due to animal respiration are removed from microvasculature imaging data. This means that only the molecular imaging data is subject to the effects of motion artifacts. However, the fact that results indicate meaningful spatial relationships between vessel diameter and distance to targeting sites (Fig. 8) suggests that any motion effects in the molecular imaging datasets are sufficiently small as to permit this type of analysis with the current system.

The use of chirped excitation may be an alternative means for improving sensitivity to bound microbubbles, which has previously been demonstrated in contrast imaging (Borsboom et al. 2005; Sun et al. 2006; Leavens et al. 2007; Sun et al. 2007). While this may enable molecular imaging of microbubbles of varying diameters at lower peak pressures, these pulses have not been assessed in superharmonic contrast imaging, in which the highest amplitude echoes are produced by microbubble destruction (Lindsey et al. 2015). This suggests that short pulses may be more effective for superharmonic imaging because they induce microbubble destruction over a smaller volume than longer pulses. Use of chirped pulses also depends on the ability of the transducer to transmit a pulse without distortion (Lindsey et al. 2015).

### Value of combined molecular and vascular imaging

The combination of molecular imaging and acoustic angiography provides opportunities for investigating the spatial distribution of functional biomarkers and vascular structures in concert. Given that ultrasound molecular imaging utilizes vascular targets, combining ultrasound molecular imaging with angiography images mapping vascular structure provides the unique opportunity to analyze relationships between vascular features and molecular information. In this work, we have observed that cyclic RGD microbubbles targeted to the $\alpha_v\beta_3$ integrin were detected preferentially in smaller vessels, and that all targeting sites were located within 200 μm of a resolvable vessel, with the majority of targeting occurring within 50 μm of a segmented vessel. Molecular targeting may be increased in small vessels due to slower blood flow velocities or the increasing similarity between microbubble and vessel diameters, which may improve the probability of binding (Takalkar et al. 2004; Kaufmann et al. 2007). Alternatively, binding in larger vessels may prove transient or more challenging due to detachment caused by greater shear flow, with binding efficiency in shear flow also dependent upon ligand concentration on the microbubble surface (Klibanov et al. 2006; Patil et al. 2011). Smaller vessels may also retain bubbles which detach due to either shear flow or ultrasound for a longer time period.

However, straightforward relationships between vessel diameter and flow rate do not hold in tumors due to the formation of abnormal vascular networks created by tumor angiogenesis (Jain 1988). The spatial distribution of integrin expression may also vary with vessel diameter, as previous investigations have reported that molecular targets of angiogenesis, such as vascular endothelial growth factor (VEGF) or the $\alpha_v\beta_3$ integrin used in this work may be more prevalent in small vessels undergoing active remodeling (Brooks et al. 1994). While the exact relationship between vessel anatomy and molecular targeting is unclear, the

presented approach has demonstrated an initial ability to assess the sizes of vessels in which targeting occurs in pre-clinical studies.

Clinical translation of the described technique would be aided by developments in both scanning system and contrast agent technology. While there are no fundamental limitations which prevent the mechanically-steered dual-frequency transducer from being used clinically for superharmonic imaging, a dual-frequency array transducer would allow for greater control over the pressure field, ensuring a more uniform point spread function over a larger field of view while maintaining the contrast-to-tissue ratio and spatial resolution of the presented images. Clinical use of ultrasound molecular imaging is presently limited by the lack of FDA-approved targeted microbubble contrast agents, however, clinically translatable contrast agents have recently been developed such as BR55 from Bracco (Pochon et al. 2010; Pysz et al. 2010). Once targeted contrast agents are developed and approved, the described technique for superharmonic molecular imaging could enable ultrasound molecular imaging with higher resolution in all the applications currently under investigation including angiogenesis (Pochon et al. 2010), inflammation (Wang et al. 2013), and cancers of the breast (Bachawal et al. 2013), colon (Wang et al. 2015a), and prostate (Tardy et al. 2010). Combining a higher resolution molecular image with a registered angiography-like image provides additional information on microvascular morphology relative to the previously demonstrated ultrasound molecular images for these applications, in which molecular images are displayed against a background B-mode image.

In addition, the ability to visualize both microvascular anatomy and molecular targeting may also be of clinical use by providing currently unavailable information on the growth and extent of an individual tumor. For example, imaging $\alpha_v\beta_3$ expression has previously been demonstrated using PET and SPECT in tumors of the breast and brain (Bach-Gansmo et al. 2006; Beer et al. 2008; Schnell et al. 2009), and also using near-infrared fluorescence imaging in colorectal tumors (Verbeek et al. 2014). The PET imaging studies utilized an $^{18}$F-cyclic RGD tracer and then validated imaging results using post-resection immunohistochemistry, finding that while $\alpha_v\beta_3$ imaging is effective at locating tumors, its expression is “highly variable” (Beer et al. 2008; Schnell et al. 2009). While this heterogeneous expression of $\alpha_v\beta_3$ and the poor spatial resolution of PET make it difficult to use PET alone as either a screening test or a surgical planning tool, the high resolution 3D vascular and targeting information provided by acoustic angiography could make for an excellent tool for surgical planning after initial tumor localization. In this case, the expression of $\alpha_v\beta_3$ on both endothelial and tumor cells, as identified in prior PET studies (Beer et al. 2008), could prove helpful for ensuring resection with clean margins.

## Conclusions

We have presented an ultrasound-based approach for both imaging vasculature and molecular markers with high spatial resolution. This technique uses a prototype dual-frequency transducer to acquire only superharmonic signals produced by microbubble contrast agents. Although the imaging process was observed to produce decreasing image brightness over time *in vitro* due to destruction of bound microbubbles, combinations of transmit pressure and frequency can be chosen which prolong microbubble persistence.

Under such parameters, diagnostically useful superharmonic molecular images may be acquired. In this study, we have demonstrated high resolution superharmonic molecular imaging in a rodent tumor model (fibrosarcoma) using microbubbles targeted to the $\alpha_v\beta_3$ integrin. A second scan of free microbubbles was acquired immediately following the molecular scan, and the two imaging volumes were fused to provide 3D visualization of both microvascular anatomy and biodistribution of the $\alpha_v\beta_3$ integrin. Mapping both biomarkers and microvascular anatomy with high resolution provides a new method for visualizing molecular markers with ultrasound while using ultrasound-based angiography-like mapping to provide anatomical information. The combined information provided by these scans may present new opportunities for analyzing relationships between microvascular anatomy and vascular targets for microbubbles such as integrins, selectins, and other extracellular binding domains.

## Acknowledgments

This research was supported by National Institutes of Health 1R01CA170665, as well as training grant T32HL069768. We thank Mike Lee, Emmanuel Cherin, and Chris Chaggares for their contributions to the design and fabrication of prototype transducers. We would also like to acknowledge Elizabeth Bullitt and Stephen R. Aylward for guidance and algorithms for vessel segmentation. Paul Dayton declares that he has equity in SonoVol Inc., which has licensed some of the technology described in this manuscript.

## References

Anderson CR, Hu X, Zhang H, Tlaxca J, Decleves AE, Houghtaling R, Sharma K, Lawrence M, Ferrara KW, Rychak JJ. Ultrasound molecular imaging of tumor angiogenesis with an integrin targeted microbubble contrast agent. Investigative radiology. 2011; 46:215–24. [PubMed: 21343825]

Aylward SR, Bullitt E. Initialization, noise, singularities, and scale in height ridge traversal for tubular object centerline extraction. IEEE transactions on medical imaging. 2002; 21:61–75. [PubMed: 11929106]

Bach-Gansmo T, Danielsson R, Saracco A, Wilczek B, Bogsrud TV, Fangberget A, Tangerud A, Tobin D. Integrin receptor imaging of breast cancer: a proof-of-concept study to evaluate 99mTc-NC100692. J Nucl Med. 2006; 47:1434–9. [PubMed: 16954550]

Bachawal SV, Jensen KC, Lutz AM, Gambhir SS, Tranquart F, Tian L, Willmann JK. Earlier detection of breast cancer with ultrasound molecular imaging in a transgenic mouse model. Cancer research. 2013; 73:1689–98. [PubMed: 23328585]

Beer AJ, Niemeyer M, Carlsen J, Sarbia M, Nahrig J, Watzlowik P, Wester HJ, Harbeck N, Schwaiger M. Patterns of alphavbeta3 expression in primary and metastatic human breast cancer as shown by 18F-Galacto-RGD PET. J Nucl Med. 2008; 49:255–9. [PubMed: 18199623]

Borsboom JM, Chin CT, Bouakaz A, Versluis M, de Jong N. Harmonic chirp imaging method for ultrasound contrast agent. IEEE transactions on ultrasonics, ferroelectrics, and frequency control. 2005; 52:241–9.

Bouakaz A, Frigstad S, Ten Cate FJ, de Jong N. Super harmonic imaging: A new imaging technique for improved contrast detection. Ultrasound in Medicine and Biology. 2002; 28:59–68. [PubMed: 11879953]

Bouakaz A, Krenning BJ, Vletter WB, ten Cate FJ, De Jong N. Contrast superharmonic imaging: a feasibility study. Ultrasound in medicine & biology. 2003; 29:547–53. [PubMed: 12749924]

Brooks PC, Montgomery AM, Rosenfeld M, Reisfeld RA, Hu T, Klier G, Cheresh DA. Integrin alpha v beta 3 antagonists promote tumor regression by inducing apoptosis of angiogenic blood vessels. Cell. 1994; 79:1157–64. [PubMed: 7528107]

Caskey CF, Stieger SM, Qin S, Dayton PA, Ferrara KW. Direct observations of ultrasound microbubble contrast agent interaction with the microvessel wall. Journal of the Acoustical Society of America. 2007; 122:1191–200. [PubMed: 17672665]

Cerfolio RJ, Ojha B, Bryant AS, Raghuveer V, Mountz JM, Bartolucci AA. The accuracy of integrated PET-CT compared with dedicated PET alone for the staging of patients with nonsmall cell lung cancer. The Annals of thoracic surgery. 2004; 78:1017–23. discussion -23. [PubMed: 15337041]

Dayton PA, Pearson D, Clark J, Simon S, Schumann PA, Zutshi R, Matsunaga TO, Ferrara KW. Ultrasonic analysis of peptide- and antibody-targeted microbubble contrast agents for molecular imaging of alphavbeta3-expressing cells. Mol Imaging. 2004; 3:125–34. [PubMed: 15296677]

Denbeigh JM, Nixon BA, Hudson JM, Puri MC, Foster FS. VEGFR2-targeted molecular imaging in the mouse embryo: an alternative to the tumor model. Ultrasound in medicine & biology. 2014; 40:389–99. [PubMed: 24342913]

Doinikov AA, Haac JF, Dayton PA. Resonance frequencies of lipid-shelled microbubbles in the regime of nonlinear oscillations. Ultrasonics. 2009; 49:263–8. [PubMed: 18977009]

Dunleavey JM, Xiao L, Thompson J, Kim MM, Shields JM, Shelton SE, Irvin DM, Brings VE, Ollila DW, Brekken RA, Dayton PA, Melero-Martin JM, Dudley AC. Vascular channels formed by subpopulations of PECAM1+ melanoma cells. Nature communications. 2014; 5:5200.

Ellegala DB, Leong-Poi H, Carpenter JE, Klibanov AL, Kaul S, Shaffrey ME, Sklenar J, Lindner JR. Imaging tumor angiogenesis with contrast ultrasound and microbubbles targeted to alpha(v)beta3. Circulation. 2003; 108:336–41. [PubMed: 12835208]

Faez T, Goertz D, De Jong N. Characterization of Definity ultrasound contrast agent at frequency range of 5–15 MHz. Ultrasound in medicine & biology. 2011; 37:338–42. [PubMed: 21257093]

Feshitan JA, Chen CC, Kwan JJ, Borden MA. Microbubble size isolation by differential centrifugation. Journal of colloid and interface science. 2009; 329:316–24. [PubMed: 18950786]

Foster FS, Hossack J, Adamson SL. Micro-ultrasound for preclinical imaging. Interface Focus. 2011; 1:576–601. [PubMed: 22866232]

Foster FS, Mehi J, Lukacs M, Hirson D, White C, Chaggares C, Needles A. A new 15–50 MHz array-based micro-ultrasound scanner for preclinical imaging. Ultrasound in medicine & biology. 2009; 35:1700–8. [PubMed: 19647922]

Garami Z, Hascsi Z, Varga J, Dinya T, Tanyi M, Garai I, Damjanovich L, Galuska L. The value of 18-FDG PET/CT in early-stage breast cancer compared to traditional diagnostic modalities with an emphasis on changes in disease stage designation and treatment plan. European journal of surgical oncology : the journal of the European Society of Surgical Oncology and the British Association of Surgical Oncology. 2012; 38:31–7.

Garbin V, Overvelde M, Dollet B, de Jong N, Lohse D, Versluis M. Unbinding of targeted ultrasound contrast agent microbubbles by secondary acoustic forces. Phys Med Biol. 2011; 56:6161–77. [PubMed: 21878709]

Gessner R, Lukacs M, Lee M, Cherin E, Foster FS, Dayton PA. High-resolution, high-contrast ultrasound imaging using a prototype dual-frequency transducer: in vitro and in vivo studies. IEEE transactions on ultrasonics, ferroelectrics, and frequency control. 2010; 57:1772–81.

Gessner RC, Aylward SR, Dayton PA. Mapping microvasculature with acoustic angiography yields quantifiable differences between healthy and tumor-bearing tissue volumes in a rodent model. Radiology. 2012a; 264:733–40. [PubMed: 22771882]

Gessner RC, Frederick CB, Foster FS, Dayton PA. Acoustic angiography: a new imaging modality for assessing microvasculature architecture. International journal of biomedical imaging. 2013; 2013:936593. [PubMed: 23997762]

Gessner RC, Streeter JE, Kothadia R, Feingold S, Dayton PA. An in vivo validation of the application of acoustic radiation force to enhance the diagnostic utility of molecular imaging using 3-d ultrasound. Ultrasound in medicine & biology. 2012b; 38:651–60. [PubMed: 22341052]

Helfield BL, Goertz DE. Nonlinear resonance behavior and linear shell estimates for Definity and MicroMarker assessed with acoustic microbubble spectroscopy. The Journal of the Acoustical Society of America. 2013; 133:1158–68. [PubMed: 23363132]

Hu X, Caskey CF, Mahakian LM, Kruse DE, Beegle JR, Decleves AE, Rychak JJ, Sutcliffe PL, Sharma K, Ferrara KW. In vivo validation and 3D visualization of broadband ultrasound molecular

imaging. American journal of nuclear medicine and molecular imaging. 2013; 3:336–49. [PubMed: 23901359]

Hu XW, Zheng HR, Kruse DE, Sutcliffe P, Stephens DN, Ferrara KW. A Sensitive TLRH Targeted Imaging Technique for Ultrasonic Molecular Imaging. Ieee T Ultrason Ferr. 2010; 57:305–16.

Hyvelin JM, Tardy I, Bettinger T, von Wronski M, Costa M, Emmel P, Colevret D, Bussat P, Lassus A, Botteron C, Nunn A, Frinking P, Tranquart F. Ultrasound molecular imaging of transient acute myocardial ischemia with a clinically translatable P- and E-selectin targeted contrast agent: correlation with the expression of selectins. Investigative radiology. 2014; 49:224–35. [PubMed: 24442162]

Inaba Y, Lindner JR. Molecular imaging of disease with targeted contrast ultrasound imaging. Translational research : the journal of laboratory and clinical medicine. 2012; 159:140–8. [PubMed: 22340763]

Jain RK. Determinants of tumor blood flow: a review. Cancer research. 1988; 48:2641–58. [PubMed: 3282647]

Kaufmann BA, Lindner JR. Molecular imaging with targeted contrast ultrasound. Current opinion in biotechnology. 2007; 18:11–6. [PubMed: 17241779]

Kaufmann BA, Sanders JM, Davis C, Xie A, Aldred P, Sarembock IJ, Lindner JR. Molecular imaging of inflammation in atherosclerosis with targeted ultrasound detection of vascular cell adhesion molecule-1. Circulation. 2007; 116:276–84. [PubMed: 17592078]

Khismatullin DB. Resonance frequency of microbubbles: effect of viscosity. The Journal of the Acoustical Society of America. 2004; 116:1463–73. [PubMed: 15478411]

Klibanov AL, Rychak JJ, Yang WC, Alikhani S, Li B, Acton S, Lindner JR, Ley K, Kaul S. Targeted ultrasound contrast agent for molecular imaging of inflammation in high-shear flow. Contrast media & molecular imaging. 2006; 1:259–66. [PubMed: 17191766]

Kruse DE, Ferrara KW. A new imaging strategy using wideband transient response of ultrasound contrast agents. Ieee T Ultrason Ferr. 2005; 52:1320–9.

Leavens C, Williams R, Foster FS, Burns PN, Sherar MD. Golay pulse encoding for microbubble contrast imaging in ultrasound. IEEE transactions on ultrasonics, ferroelectrics, and frequency control. 2007; 54:2082–90.

Leong-Poi H, Christiansen J, Heppner P, Lewis CW, Klibanov AL, Kaul S, Lindner JR. Assessment of endogenous and therapeutic arteriogenesis by contrast ultrasound molecular Imaging of integrin expression. Circulation. 2005; 111:3248–54. [PubMed: 15956135]

Leong-Poi H, Christiansen J, Klibanov AL, Kaul S, Lindner JR. Noninvasive assessment of angiogenesis by ultrasound and microbubbles targeted to alpha(v)-integrins. Circulation. 2003; 107:455–60. [PubMed: 12551871]

Lerman H, Lievshitz G, Zak O, Metser U, Schneebaum S, Even-Sapir E. Improved sentinel node identification by SPECT/CT in overweight patients with breast cancer. J Nucl Med. 2007; 48:201–6. [PubMed: 17268015]

Lindsey BD, Rojas JD, Martin KH, Shelton SE, Dayton PA. Acoustic characterization of contrast-to-tissue ratio and axial resolution for dual-frequency contrast-specific acoustic angiography imaging. IEEE transactions on ultrasonics, ferroelectrics, and frequency control. 2014; 61:1668–87.

Lindsey BD, Shelton SE, Dayton PA. Optimization of contrast-to-tissue ratio through pulse windowing in dual-frequency "acoustic angiography" imaging. Ultrasound in medicine & biology. 2015; 41:1884–95. [PubMed: 25819467]

Liu H, Chen Y, Yan F, Han X, Wu J, Liu X, Zheng H. Ultrasound molecular imaging of vascular endothelial growth factor receptor 2 expression for endometrial receptivity evaluation. Theranostics. 2015; 5:206–17. [PubMed: 25553109]

Liu H, Jiang YX, Liu JB, Zhu QL, Sun Q. Evaluation of breast lesions with contrast-enhanced ultrasound using the microvascular imaging technique: Initial observations. Breast. 2008; 17:532–9. [PubMed: 18534851]

Loughran J, Sennoga C, R JE, Tang MX. Effect of ultrasound on adherent microbubble contrast agents. Phys Med Biol. 2012; 57:6999–7014. [PubMed: 23044731]

Martin KH, Lindsey BD, Ma J, Lee M, Li S, Foster FS, Jiang X, Dayton PA. Dual-Frequency Piezoelectric Transducers for Contrast Enhanced Ultrasound Imaging. Sensors. 2014; 14:20825–42. [PubMed: 25375755]

Patil AV, Rychak JJ, Klibanov AL, Hossack JA. Real-time technique for improving molecular imaging and guiding drug delivery in large blood vessels: in vitro and ex vivo results. Mol Imaging. 2011; 10:238–47. [PubMed: 21521555]

Pochon S, Tardy I, Bussat P, Bettinger T, Brochot J, von Wronski M, Passantino L, Schneider M. BR55: a lipopeptide-based VEGFR2-targeted ultrasound contrast agent for molecular imaging of angiogenesis. Investigative radiology. 2010; 45:89–95. [PubMed: 20027118]

Pysz MA, Foygel K, Panje CM, Needles A, Tian L, Willmann JK. Assessment and monitoring tumor vascularity with contrast-enhanced ultrasound maximum intensity persistence imaging. Investigative radiology. 2011; 46:187–95. [PubMed: 21150790]

Pysz MA, Foygel K, Rosenberg J, Gambhir SS, Schneider M, Willmann JK. Antiangiogenic cancer therapy: monitoring with molecular US and a clinically translatable contrast agent (BR55). Radiology. 2010; 256:519–27. [PubMed: 20515975]

Roach PJ, Schembri GP, Shon IAH, Bailey EA, Bailey DL. SPECT/CT imaging using a spiral CT scanner for anatomical localization: Impact on diagnostic accuracy and reporter confidence in clinical practice. Nucl Med Commun. 2006; 27:977–87. [PubMed: 17088684]

Rychak JJ, Graba J, Cheung AM, Mystry BS, Lindner JR, Kerbel RS, Foster FS. Microultrasound molecular imaging of vascular endothelial growth factor receptor 2 in a mouse model of tumor angiogenesis. Mol Imaging. 2007; 6:289–96. [PubMed: 18092513]

Sassaroli E, Hynynen K. Forced linear oscillations of microbubbles in blood capillaries. The Journal of the Acoustical Society of America. 2004; 115:3235–43. [PubMed: 15237848]

Satinover SJ, Dove JD, Borden MA. Single-particle optical sizing of microbubbles. Ultrasound in medicine & biology. 2014; 40:138–47. [PubMed: 24139917]

Schnell O, Krebs B, Carlsen J, Miederer I, Goetz C, Goldbrunner RH, Wester HJ, Haubner R, Popperl G, Holtmannspotter M, Kretzschmar HA, Kessler H, Tonn JC, Schwaiger M, Beer AJ. Imaging of integrin alpha(v)beta(3) expression in patients with malignant glioma by [18F] Galacto-RGD positron emission tomography. Neuro-oncology. 2009; 11:861–70. [PubMed: 19401596]

Shelton SE, Lee YZ, Foster FS, Lee M, Cherin E, Aylward SR, Dayton PA. Quantification of microvascular tortuosity during tumor evolution utilizing acoustic angiography. Ultrasound in medicine & biology. 2015 Accepted for publication:

Sirsi S, Feshitan J, Kwan J, Homma S, Borden M. Effect of microbubble size on fundamental mode high frequency ultrasound imaging in mice. Ultrasound in medicine & biology. 2010; 36:935–48. [PubMed: 20447755]

Soyka JD, Muster MA, Schmid DT, Seifert B, Schick U, Miralbell R, Jorcano S, Zaugg K, Seifert HH, Veit-Haibach P, Strobel K, Schaefer NG, Husarik DB, Hany TF. Clinical impact of 18F-choline PET/CT in patients with recurrent prostate cancer. Eur J Nucl Med Mol Imaging. 2012; 39:936–43. [PubMed: 22415598]

Sternberg S. Biomedical Image Processing. Computer. 1983; 16:22–34.

Streeter JE, Dayton PA. An in vivo evaluation of the effect of repeated administration and clearance of targeted contrast agents on molecular imaging signal enhancement. Theranostics. 2013; 3:93–8. [PubMed: 23424189]

Streeter JE, Gessner R, Miles I, Dayton PA. Improving sensitivity in ultrasound molecular imaging by tailoring contrast agent size distribution: in vivo studies. Mol Imaging. 2010; 9:87–95. [PubMed: 20236606]

Streeter JE, Gessner RC, Tsuruta J, Feingold S, Dayton PA. Assessment of molecular imaging of angiogenesis with three-dimensional ultrasonography. Mol Imaging. 2011; 10:460–8. [PubMed: 22201537]

Sun Y, Kruse DE, Ferrara KW. Contrast imaging with chirped excitation. IEEE transactions on ultrasonics, ferroelectrics, and frequency control. 2007; 54:520–9.

Sun Y, Zhao S, Dayton PA, Ferrara KW. Observation of contrast agent response to chirp insonation with a simultaneous optical-acoustical system. IEEE transactions on ultrasonics, ferroelectrics, and frequency control. 2006; 53:1130–7.

Takalkar AM, Klibanov AL, Rychak JJ, Lindner JR, Ley K. Binding and detachment dynamics of microbubbles targeted to P-selectin under controlled shear flow. Journal of controlled release : official journal of the Controlled Release Society. 2004; 96:473–82. [PubMed: 15120903]

Talu E, Hettiarachchi K, Zhao S, Powell RL, Lee AP, Longo ML, Dayton PA. Tailoring the size distribution of ultrasound contrast agents: possible method for improving sensitivity in molecular imaging. Mol Imaging. 2007; 6:384–92. [PubMed: 18053409]

Tardy I, Pochon S, Theraulaz M, Emmel P, Passantino L, Tranquart F, Schneider M. Ultrasound Molecular Imaging of VEGFR2 in a Rat Prostate Tumor Model Using BR55. Investigative radiology. 2010; 45:573–8. [PubMed: 20808233]

Tharp K, Israel O, Hausmann J, Bettman L, Martin WH, Daitzchman M, Sandler MP, Delbeke D. Impact of I-131-SPECT/CT images obtained with an integrated system in the follow-up of patients with thyroid carcinoma. Eur J Nucl Med Mol I. 2004; 31:1435–42.

Verbeek FPR, van der Vorst JR, Tummers QRJG, Boonstra MC, de Rooij KE, Lowik CWGM, Valentijn ARPM, van de Velde CJH, Choi HS, Frangioni JV, Vahrmeijer AL. Near-Infrared Fluorescence Imaging of Both Colorectal Cancer and Ureters Using a Low-Dose Integrin Targeted Probe. Ann Surg Oncol. 2014; 21:S528–S37. [PubMed: 24515567]

Voigt JU. Ultrasound molecular imaging. Methods. 2009; 48:92–7. [PubMed: 19324089]

Wang H, Kaneko OF, Tian L, Hristov D, Willmann JK. Three-Dimensional Ultrasound Molecular Imaging of Angiogenesis in Colon Cancer Using a Clinical Matrix Array Ultrasound Transducer. Investigative radiology. 2015a

Wang H, Machtaler S, Bettinger T, Lutz AM, Luong R, Bussat P, Gambhir SS, Tranquart F, Tian L, Willmann JK. Molecular imaging of inflammation in inflammatory bowel disease with a clinically translatable dual-selectin-targeted US contrast agent: comparison with FDG PET/CT in a mouse model. Radiology. 2013; 267:818–29. [PubMed: 23371306]

Wang SY, Hossack JA, Klibanov AL, Mauldin FW. Binding dynamics of targeted microbubbles in response to modulated acoustic radiation force. Phys Med Biol. 2014; 59:465–84. [PubMed: 24374866]

Wang SY, Mauldin FW, Klibanov AL, Hossack JA. Ultrasound-Based Measurement of Molecular Marker Concentration in Large Blood Vessels: A Feasibility Study. Ultrasound in Medicine and Biology. 2015b; 41:222–34. [PubMed: 25308943]

Willmann JK, Kimura RH, Deshpande N, Lutz AM, Cochran JR, Gambhir SS. Targeted Contrast-Enhanced Ultrasound Imaging of Tumor Angiogenesis with Contrast Microbubbles Conjugated to Integrin-Binding Knottin Peptides. J Nucl Med. 2010; 51:433–40. [PubMed: 20150258]

Willmann JK, Paulmurugan R, Chen K, Gheysens O, Rodriguez-Porcel M, Lutz AM, Chen IY, Chen X, Gambhir SS. US imaging of tumor angiogenesis with microbubbles targeted to vascular endothelial growth factor receptor type 2 in mice. Radiology. 2008; 246:508–18. [PubMed: 18180339]

Yan F, Li X, Jin Q, Chen J, Shandas R, Wu J, Li L, Ling T, Yang W, Chen Y, Liu X, Zheng H. Ultrasonic imaging of endothelial CD81 expression using CD81-targeted contrast agents in in vitro and in vivo studies. Ultrasound in medicine & biology. 2012; 38:670–80. [PubMed: 22341598]

Yuan H, Schroeder T, Bowsher JE, Hedlund LW, Wong T, Dewhirst MW. Intertumoral differences in hypoxia selectivity of the PET imaging agent 64Cu(II)-diacetyl-bis(N4-methylthiosemicarbazone). J Nucl Med. 2006; 47:989–98. [PubMed: 16741309]

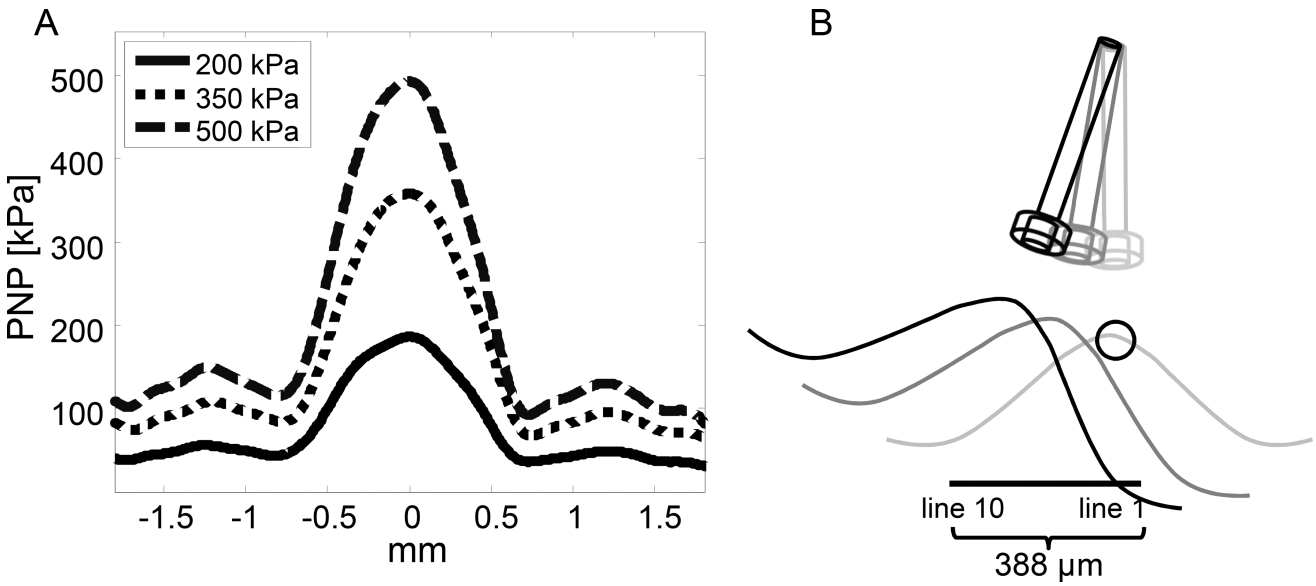


**Figure 1.**

**(A)** Hydrophone-measured pressure maps as a transmit beam having a peak negative pressure of 200 kPa (solid line), 350 kPa (dotted line), or 500 kPa (dashed line) is swept from left to right. **(B)** Motion of transducer mechanical arm for the scenario in Fig. 1A. Illustration of transmitted pressure experienced by a single microbubble as the mechanically steered transducer arm moves from some distance away from the bubble (gray) to on-axis steering (black). Given a line separation of 43.1 µm, 10 adjacent lines occupy a distance of 387.9 µm, over which a single bubble is exposed to multiple pulses of gradually increasing pressure until the on-axis bubble experiences the nominal peak negative pressure.

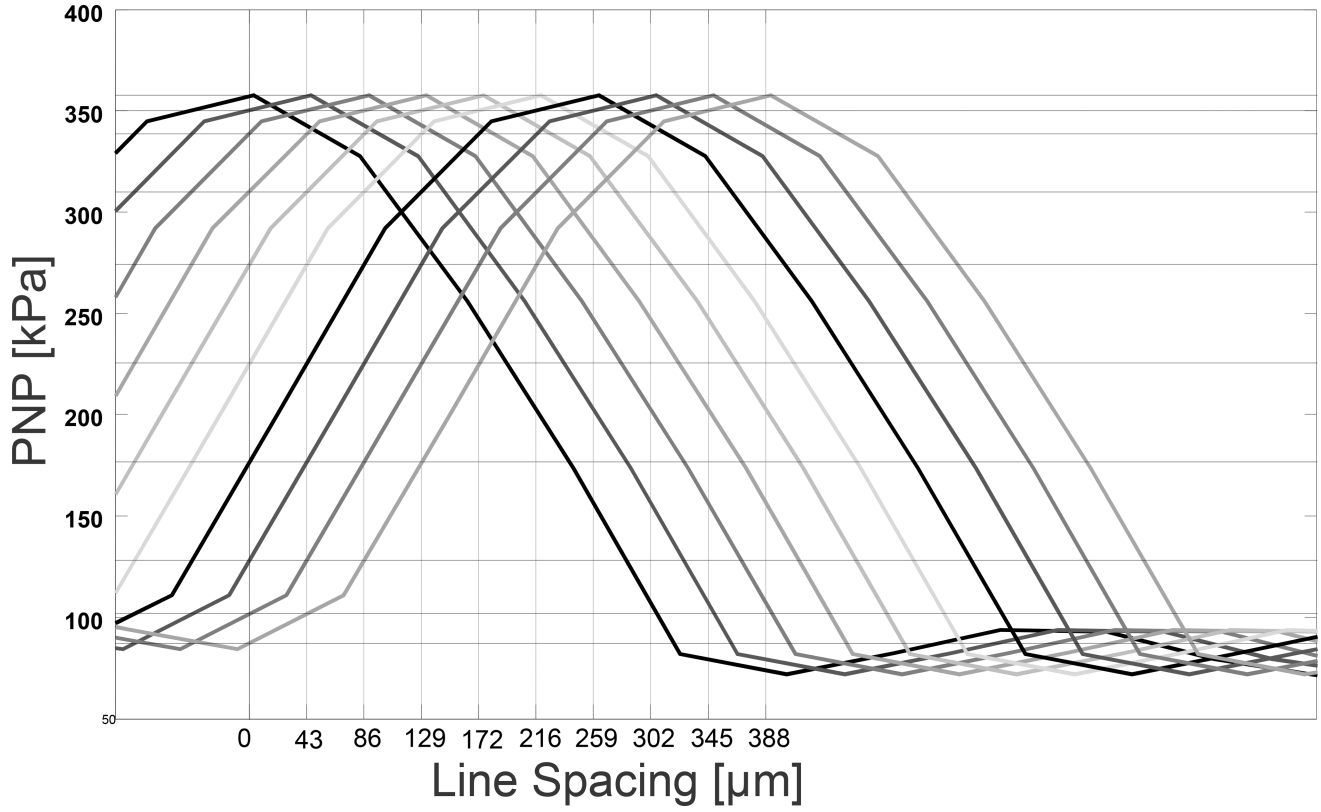


**Figure 2.**

Peak negative pressures (horizontal lines) in kPa experienced by a bubble at position 0, due to 10 adjacent scan lines with a line spacing of 43.1 μm (illustrated by the vertical lines).

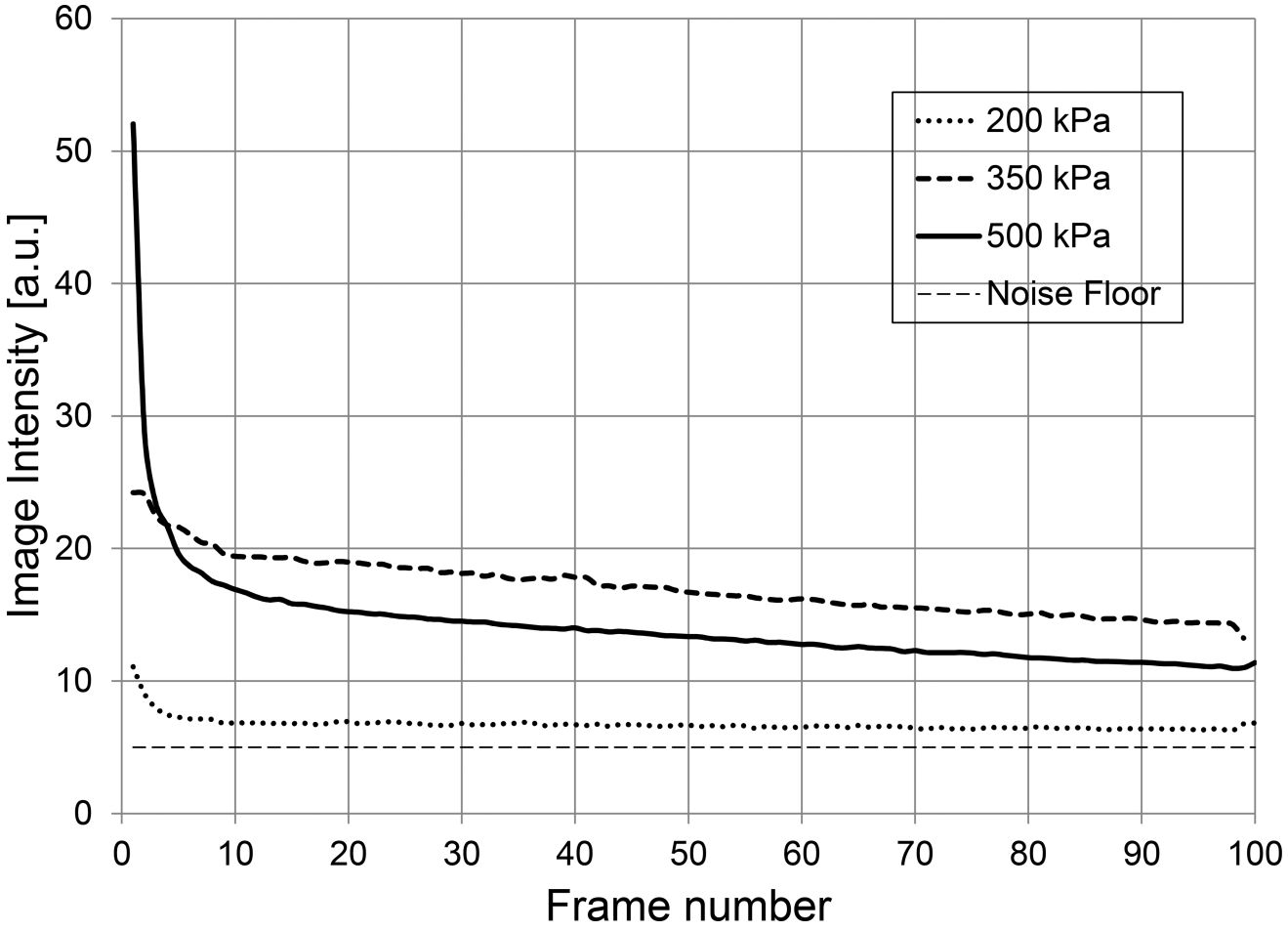


**Figure 3.**
Image intensity vs. frame number for targeted biotin microbubbles adhered to an avidin-coated tube. Each line indicates the mean result of 3 experiments.

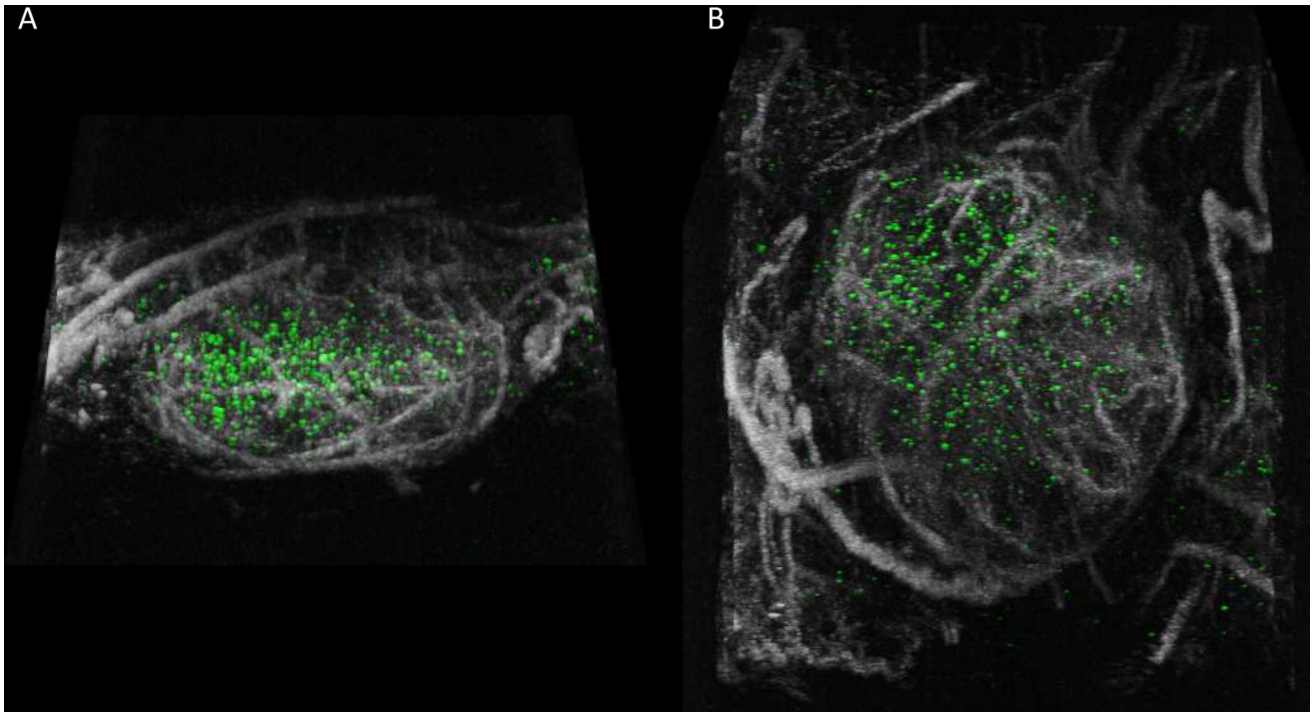


**Figure 4.**

**(A)** Fused scans of vascular anatomy acquired using untargeted (grayscale) and cyclic RGD microbubbles (green) in sequential scans of a subcutaneous fibrosarcoma in the same animal. Images are shown here in a lateral view. **(B)** The same data in (A) is shown in a dorsal-ventral view. Both scale bars represent 2 mm.

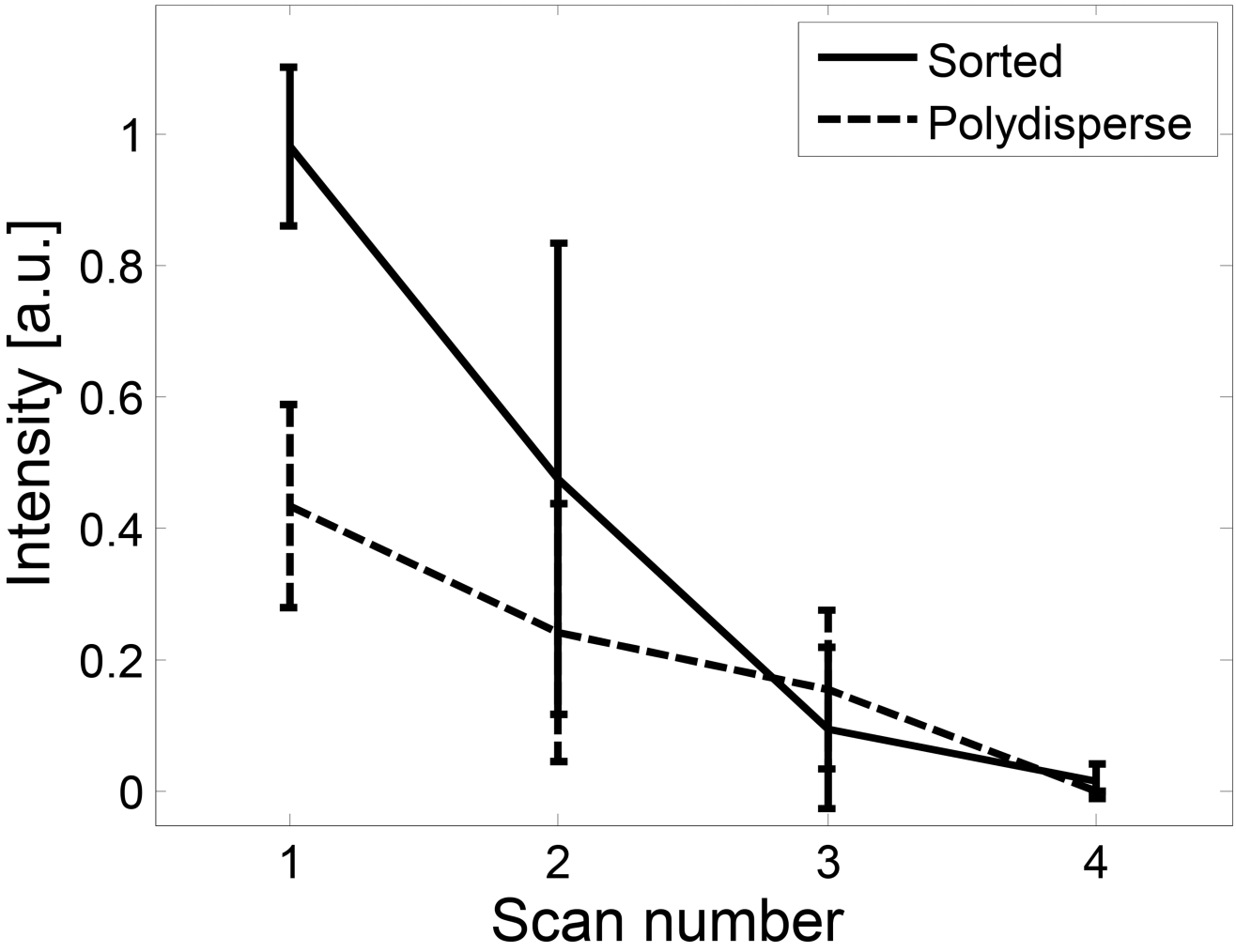


**Figure 5.**
Image intensity over 4 consecutive scans with cyclic RGD bubbles in n=5 animals at non-derated peak negative transmit pressures of 1200 kPa for both sorted and polydisperse cyclic RGD microbubble populations. Each scan was normalized to its initial intensity.

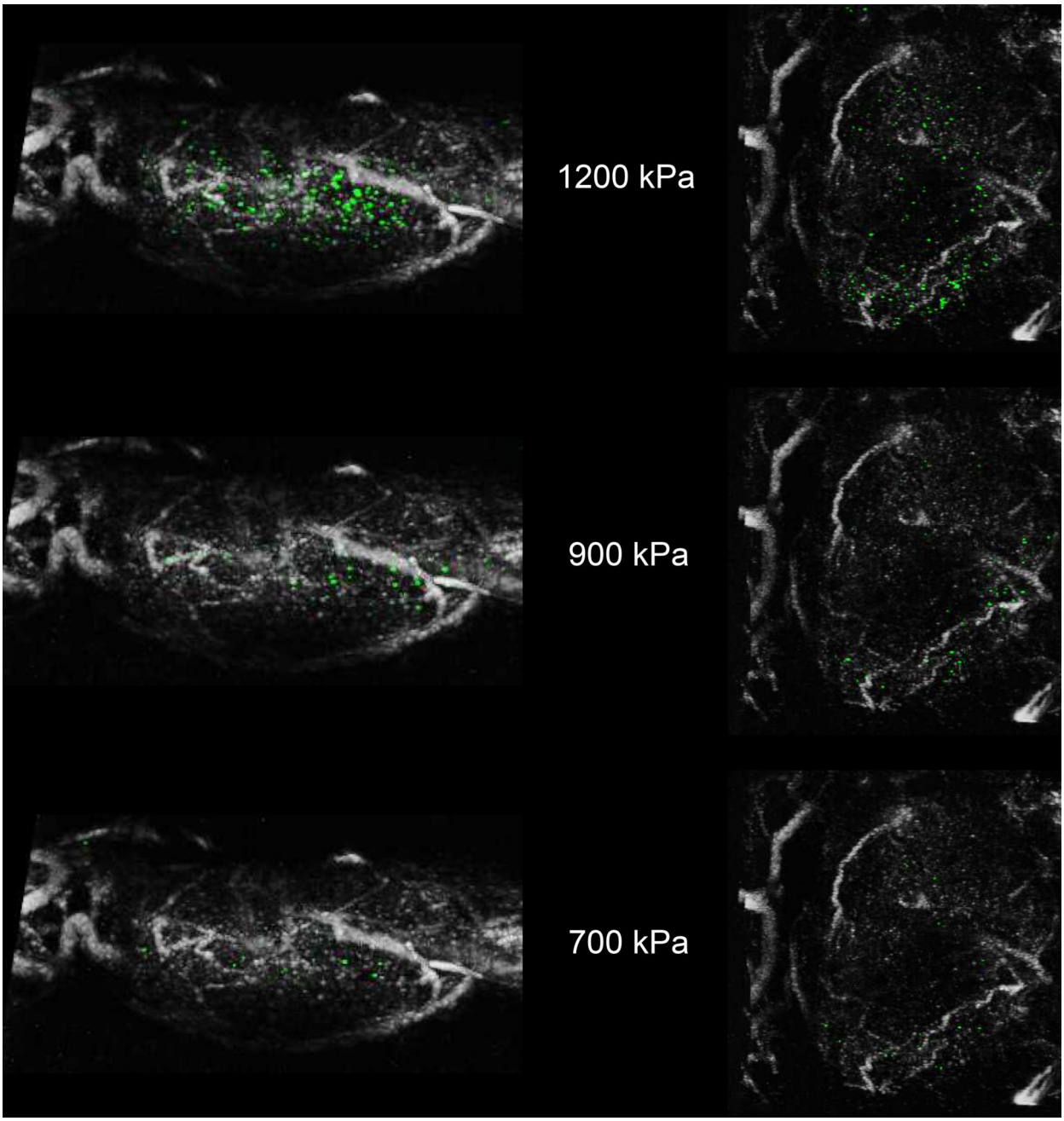


**Figure 6.**

The effect of varying peak transmit pressure on received molecular imaging signal (green) is illustrated in a single animal in both lateral (left) and dorsal-ventral views (right). The same acoustic angiography data (grayscale) was used to provide vascular anatomy for all cases.

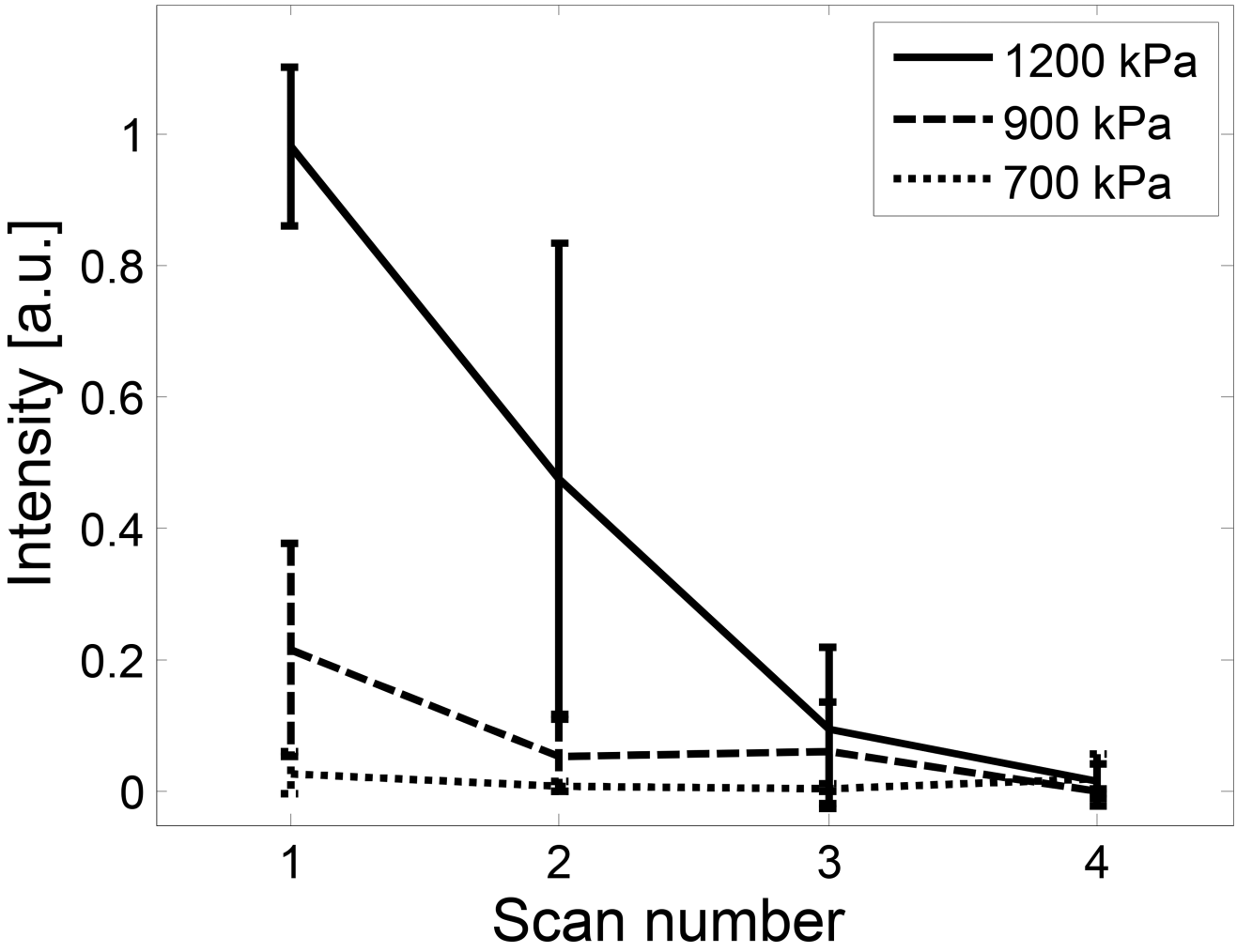


**Figure 7.**
Image intensity over 4 consecutive scans with cyclic RGD bubbles in n=5 animals with varying peak negative transmit pressures of 700, 900, and 1200 kPa for size-sorted microbubble populations. Each scan was normalized to its initial intensity.

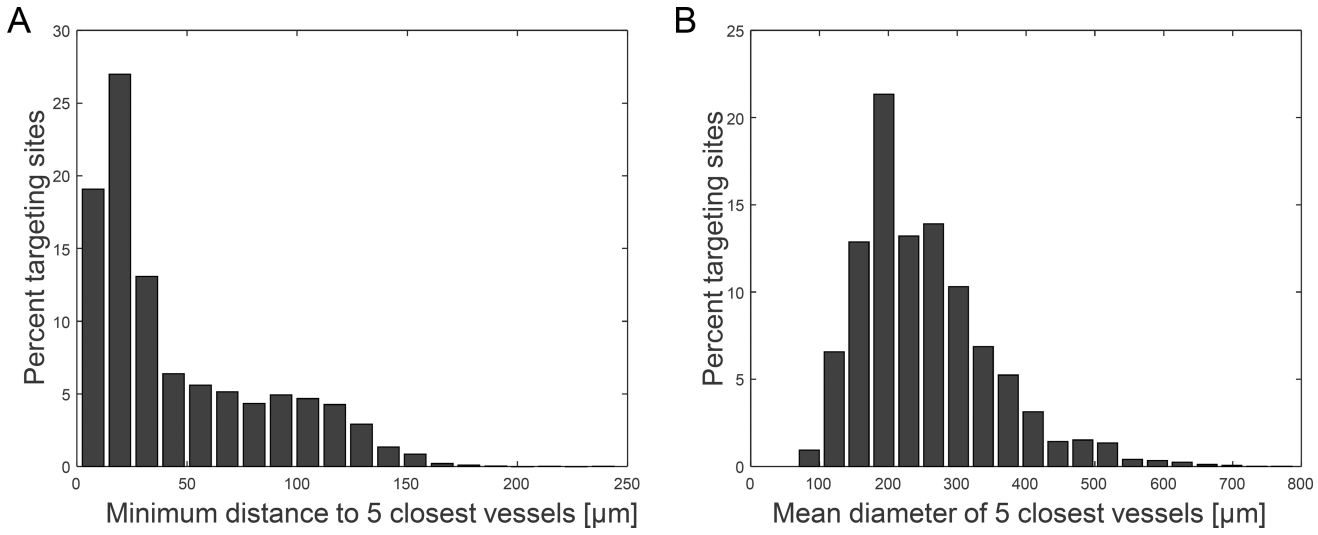


**Figure 8.**

Histograms of (A) the distance to the 5 closest resolvable vessels and (B) the mean diameter of these vessels in n=5 animals indicate that most targeting occurred close to a vessel approximately 100–300 μm in diameter.